

Crystal growth, structure, and physical properties of $\text{Ln}(\text{Cu,Al})_{12}$ (Ln = Y, Ce, Pr, Sm, and Yb) and $\text{Ln}(\text{Cu,Ga})_{12}$ (Ln = Y, Gd–Er, and Yb)

This article has been downloaded from IOPscience. Please scroll down to see the full text article.

2010 J. Phys.: Condens. Matter 22 066001

(<http://iopscience.iop.org/0953-8984/22/6/066001>)

View [the table of contents for this issue](#), or go to the [journal homepage](#) for more

Download details:

IP Address: 129.252.86.83

The article was downloaded on 30/05/2010 at 07:06

Please note that [terms and conditions apply](#).

Crystal growth, structure, and physical properties of $\text{Ln}(\text{Cu}, \text{Al})_{12}$ ($\text{Ln} = \text{Y}, \text{Ce}, \text{Pr}, \text{Sm}, \text{and Yb}$) and $\text{Ln}(\text{Cu}, \text{Ga})_{12}$ ($\text{Ln} = \text{Y}, \text{Gd–Er}, \text{and Yb}$)

Brenton L Drake¹, C Capan², Jung Young Cho¹, Y Nambu³,
K Kuga³, Y M Xiong³, A B Karki², S Nakatsuji³, P W Adams³,
D P Young² and Julia Y Chan^{1,4}

¹ Department of Chemistry, Louisiana State University, Baton Rouge, LA 70803, USA

² Department of Physics and Astronomy, Louisiana State University, Baton Rouge, LA 70803, USA

³ Institute for Solid State Physics, University of Tokyo, Kashiwa 277-8581, Japan

E-mail: jchan@lsu.edu

Received 26 October 2009, in final form 10 December 2009

Published 27 January 2010

Online at stacks.iop.org/JPhysCM/22/066001

Abstract

Single crystals of $\text{Ln}(\text{Cu}, \text{Al})_{12}$ and $\text{Ln}(\text{Cu}, \text{Ga})_{12}$ compounds ($\text{Ln} = \text{Y}, \text{Ce–Nd}, \text{Sm}, \text{Gd–Ho}$, and Yb for Al and $\text{Ln} = \text{Y}, \text{Gd–Er}, \text{Yb}$ for Ga) have been grown by flux-growth methods and characterized by means of single-crystal x-ray diffraction, complemented with microprobe analysis, magnetic susceptibility, resistivity and heat capacity measurements. $\text{Ln}(\text{Cu}, \text{Ga})_{12}$ and $\text{Ln}(\text{Cu}, \text{Al})_{12}$ of the ThMn_{12} structure type crystallize in the tetragonal $I4/mmm$ space group with lattice parameters $a \sim 8.59 \text{ \AA}$ and $c \sim 5.15 \text{ \AA}$ and $a \sim 8.75 \text{ \AA}$ and $c \sim 5.13 \text{ \AA}$ for Ga and Al containing compounds, respectively. For aluminium containing compounds, magnetic susceptibility data show Curie–Weiss paramagnetism in the Ce and Pr analogues down to 50 K with no magnetic ordering down to 3 K, whereas the Yb analogue shows a temperature-independent Pauli paramagnetism. $\text{Sm}(\text{Cu}, \text{Al})_{12}$ orders antiferromagnetically at $T_N \sim 5 \text{ K}$ and interestingly exhibits Curie–Weiss behaviour down to 10 K with no Van Vleck contribution to the susceptibility. Specific heat data show that $\text{Ce}(\text{Cu}, \text{Al})_{12}$ is a heavy fermion antiferromagnet with $T_N \sim 2 \text{ K}$ and with an electronic specific heat coefficient γ_0 as large as $390 \text{ mJ K}^2 \text{ mol}^{-1}$. In addition, this is the first report of $\text{Pr}(\text{Cu}, \text{Al})_{12}$ and $\text{Sm}(\text{Cu}, \text{Al})_{12}$ showing an enhanced mass (~ 80 and $120 \text{ mJ K}^2 \text{ mol}^{-1}$). For Ga containing analogues, magnetic susceptibility data also show the expected Curie–Weiss behaviour from Gd to Er, with the Yb analogue being once again a Pauli paramagnet. The antiferromagnetic transition temperatures range over 12.5, 13.5, 6.7, and 3.4 K for Gd, Tb, Dy, and Er. Metallic behaviour is observed down to 3 K for all Ga and Al analogues. A large positive magnetoresistance up to 150% at 9 T is also observed for $\text{Dy}(\text{Cu}, \text{Ga})_{12}$. The structure, magnetic, and transport properties of these compounds will be discussed.

1. Introduction

Pseudo-binary lanthanide intermetallic compounds (Ln–T–X where $\text{Ln} = \text{lanthanide}$, $\text{T} = \text{transition metal}$, and

$\text{X} = \text{main group element}$) adopting the ThMn_{12} structure type [1, 2] have been extensively studied and show a variety of interesting physical properties including magnetism and superconductivity [3–12]. This tetragonal phase ($I4/mmm$) consists of a lanthanide, transition metal, and a main group element occupying the 2a ($4/mmm$), 8f ($2/m$), 8i ($m2m$), and

⁴ Author to whom any correspondence should be addressed.

8j ($m2m$) Wyckoff sites. It is worthy of note that the 8i and 8j positions are jointly occupied by T and X when $X = \text{Ga}$, and for $X = \text{Al}$ only 8j is jointly occupied. Growth of the pseudo-binary lanthanide analogues in this structure type is considerably stabilized with the addition of the third element, as only Mn and Zn lanthanide derivatives have been shown to crystallize in this structure type [13–16].

The magnetic ordering at low temperatures due to long-range lanthanide interactions has been reported for several compounds where $M = \text{Cr}$ or Cu and $X = \text{Al}$. CeCr_4Al_8 exhibits an enhanced Sommerfeld coefficient of specific heat, $\gamma \sim 62 \text{ mJ mol}^{-1} \text{ K}^{-1}$, and does not magnetically order down to 1.5 K [17]. GdCr_4Al_8 and ErCr_4Al_8 show antiferromagnetic (AFM) ordering around 8 K and 14 K, respectively [18, 19]. Similarly, CeCu_4Al_8 shows heavy fermion behaviour with $\gamma \sim 300 \text{ mJ mol}^{-1} \text{ K}^{-1}$ [20]. Reported on more recently, $\text{CeCu}_{4+x}\text{Al}_{8-x}$ ($0 < x < 0.55$) shows heavy fermion behaviour ($\gamma \sim 200 \text{ mJ mol}^{-1} \text{ K}^{-1}$) with antiferromagnetic ordering at 5.8 K, which was not previously observed; it was reported to be paramagnetic down to 4.1 K [19, 21–23]. HoCu_4Al_8 and ErCu_4Al_8 compounds have been shown to order antiferromagnetically at 5.5 K and 6 K, respectively, which is due to the ordering of the lanthanide sublattice, with a second report of HoCu_4Al_8 ordering at 7 K [17–19, 24].

Addition of magnetic transition metals like Fe presents possibilities for magnetic ordering due to transition metal interactions and long-range lanthanide interactions, respectively [10, 25–28]. For example, ErFe_4Al_8 shows two magnetic transitions, at 25 K and 111 K, corresponding to the ordering of the Er and Fe sublattices, respectively [26]. In addition, negative magnetoresistance in the range of -1.8% to -20.1% has been found in several of the RFe_4Al_8 compounds ($R = \text{Sc}, \text{Y}, \text{Ce}, \text{Yb}, \text{and Lu}$) [6].

We have grown $\text{Ln}(\text{Cu}, \text{Ga})_{12}$ and $\text{Ln}(\text{Cu}, \text{Al})_{12}$ analogues ($\text{Ln} = \text{Y}, \text{Gd–Er}, \text{Yb}$ for Ga and $\text{Ln} = \text{Y}, \text{Ce–Nd}, \text{Sm}, \text{Gd–Ho}, \text{and Yb}$ for Al) using Ga and Al flux-growth techniques. To the best of our knowledge, there has not been a systematic study on ThMn_{12} structure in the Ln–Cu–Ga system. In addition, during exploration of the Ln–Cu–Al system, high quality single crystals were grown that upon further study are found not to give results in agreement with some previously published ones. Here, we report the crystal growth, magnetism, and transport properties of $\text{Ln}(\text{Cu}, \text{Ga})_{12}$ and $\text{Ln}(\text{Cu}, \text{Al})_{12}$ compounds ($\text{Ln} = \text{Y}, \text{Gd–Er}, \text{Yb}$ for Ga and $\text{Ln} = \text{Y}, \text{Ce}, \text{Pr}, \text{Sm}, \text{and Yb}$ for Al).

2. Experimental details

2.1. Synthesis

Single crystals of $\text{Ln}(\text{Cu}, \text{X})_{12}$ ($\text{Ln} = \text{Y}, \text{Ce–Nd}, \text{Sm}, \text{Gd–Ho}$ and Yb for $X = \text{Al}$ (note that $\text{Ln} = \text{Ce–Nd}, \text{Sm}, \text{Gd–Ho}, \text{Yb}, \text{and Y}$ ones have been grown for $\text{Ln}(\text{Cu}, \text{Al})_{12}$ but only the properties for Ce, Pr, Sm, Yb, and Y will be reported) and $\text{Ln} = \text{Y}, \text{Gd–Er}, \text{Yb}$ ones for $X = \text{Ga}$) were grown in the presence of excess flux. Ln (3N, chunks, Alfa Aesar), Cu (5N, powder, Alfa Aesar), and Al (5N, pellets, Alfa Aesar) or Ga (6N, pellets, Alfa Aesar) were loaded, respectively, into an alumina crucible with a reaction ratio of 1:9:20

for Al containing analogues and 1:5:20 for Ga containing compounds. Elements were stored in inert atmospheres to prevent oxidation. The crucibles were placed into a fused silica tube and the contents were evacuated (50–70 mmHg) and sealed.

2.1.1. $\text{Ln}(\text{Cu}, \text{Al})_{12}$. The vessel was loaded into a furnace and heated to a dwell temperature of 1100°C for 10 h at 200°C h^{-1} . Samples were slowly cooled to 720°C at a rate of 4°C h^{-1} whereupon they were centrifuged to separate crystals from the Al flux. In attempts to increase the crystal size, Yb samples were cooled at slower ramp down temperatures ($0.5\text{--}1^\circ\text{C h}^{-1}$). Final dwell times were varied from hours to days, and it was observed that crystal size increases with dwell time. In addition, it was clearly observed that with different dwell times a differing amount of Cu was substituted into the Al site. For Yb samples, crystal size was maximized from a short dwell time, not following the general trend for the other analogues. This is possibly due to the high vapour pressure of Yb. In all growths, silver metallic crystals were retrieved via etching in NaOH (6 M) until excess aluminium was removed, and subsequently cleaned with 30% HNO_3 , yielding flux-free single crystals which were observed to be air stable.

2.1.2. $\text{Ln}(\text{Cu}, \text{Ga})_{12}$. The crucible and its contents were then sealed in an evacuated fused silica tube and heated to 1100°C for 7 h. The tube was then slowly cooled to 673°C at a rate of 10°C h^{-1} and immediately inverted and spun with a centrifuge for the removal of excess Ga flux. Silver-coloured block-like crystals were found and not observed to degrade in air. To ensure the complete removal of Ga from surfaces, crystals were etched using a diluted HCl (1 M) solution. After etching crystals for several hours, reddish colours on crystal surfaces were observed, indicating exposure of excess Cu as well as the completion of removal of Ga from crystal surfaces. The Cu was successfully removed by using a diluted HNO_3 (30%) solution.

2.2. Single-crystal x-ray diffraction, powder x-ray diffraction, and elemental analysis

The crystals of $\text{Ln}(\text{Cu}, \text{Al})_{12}$ or $\text{Ln}(\text{Cu}, \text{Ga})_{12}$ were cut to suitable sizes for data collection ($\leq 0.05 \text{ mm}^3$) and mounted on a glass fibre using epoxy. They were then positioned onto the goniometer of a Nonius Kappa CCD diffractometer equipped with $\text{Mo K}\alpha$ radiation ($\lambda = 0.71073 \text{ \AA}$). Data collection was carried out up to $\theta = 30.0^\circ$ at 298 K. Further crystallographic parameters for $\text{Ln}(\text{Cu}, \text{Al})_{12}$ ($\text{Ln} = \text{Y}, \text{Ce}, \text{Pr}, \text{Sm}$ and Yb) and $\text{Ln}(\text{Cu}, \text{Ga})_{12}$ ($\text{Ln} = \text{Y}, \text{Gd–Er}, \text{Yb}$) are provided in tables 1a and 1b. Direct methods were used to solve the structure. SHELXL97 [29] was used to refine the structural model and data were corrected with extinction coefficients and refined with anisotropic displacement parameters. Refinement assuming a fully occupied formula led to convergence with very small final difference residual peaks. Selected interatomic distances are presented in tables 2a and 2b, and atomic positions and displacements are provided in tables 3a and 3b. To determine the composition of $\text{Ln}(\text{Cu}, \text{Al})_{12}$ or $\text{Ln}(\text{Cu}, \text{Ga})_{12}$, electron

Table 1a. Crystallographic parameters for Ln(Cu, Al)₁₂.

Formula	Ce(Cu, Al) ₁₂	Pr(Cu, Al) ₁₂	Sm(Cu, Al) ₁₂	Yb(Cu, Al) ₁₂	Y(Cu, Ga) ₁₂
<i>a</i> (Å)	8.813(3)	8.792(6)	8.749(2)	8.721(3)	8.704 (3)
<i>c</i> (Å)	5.160(2)	5.156(3)	5.146(2)	5.118(2)	5.131(2)
<i>V</i> (Å ³)	400.8(2)	398.6(4)	393.9(2)	389.3(2)	388.7(2)
<i>Z</i>	2	2	2	2	2
Crystal system	Tetragonal	Tetragonal	Tetragonal	Tetragonal	Tetragonal
Space group	<i>I4/mmm</i>	<i>I4/mmm</i>	<i>I4/mmm</i>	<i>I4/mmm</i>	<i>I4/mmm</i>
θ range (deg)	3.27–30.02	3.28–29.95	3.29–29.94	3.30–29.72	3.31–28.61
μ (mm ⁻¹)	18.424	19.015	21.075	25.657	18.961
Data collection:					
Measured reflections	531	465	487	479	476
Independent reflections	196	190	191	190	169
Reflections with $I > 2\sigma(I)$	195	188	188	184	161
R_{int}	0.0581	0.0359	0.0471	0.0304	0.0525
<i>h</i>	−12 → 12	−12 → 12	−12 → 12	−12 → 12	−11 → 11
<i>k</i>	−8 → 8	−8 → 8	−8 → 8	−8 → 8	−7 → 8
<i>l</i>	−7 → 5	−6 → 5	−7 → 4	−7 → 4	−6 → 6
Refinement:					
$R_1[F^2 > 2\sigma(F^2)]^a$	0.0292	0.0262	0.021	0.0237	0.0289
$wR_2(F^2)^b$	0.0679	0.0624	0.0509	0.0542	0.0715
Reflections	196	190	191	190	169
Parameters	17	17	17	17	17
$\Delta\rho_{\text{max}}$ (e Å ⁻³)	2.293	1.239	1.487	2.928	1.088
$\Delta\rho_{\text{min}}$ (e Å ⁻³)	−1.688	−1.904	−1.69	−1.836	−0.845

$$^a R_1 = \sum |F_o| - |F_c| / \sum |F_o|.$$

$$^b wR_2 = [\sum [w(F_o^2 - F_c^2)] / \sum [w(F_o^2)^2]]^{1/2}. w = 1/[\sigma^2(F_o^2) + (0.0328P)^2 + 1.7521P],$$

$$w = 1/[\sigma^2(F_o^2) + (0.0252P)^2 + 1.7135P], w = 1/[\sigma^2(F_o^2) + (0.0085P)^2 + 0.6996P],$$

$$w = 1/[\sigma^2(F_o^2) + (0.0241P)^2 + 1.1008P], w = 1/[\sigma^2(F_o^2) + (0.0390P)^2 + 0.0000P], \text{ for Ce, Pr, Sm, Yb and Y, respectively.}$$

Table 1b. Crystallographic parameters for Ln(Cu, Ga)₁₂.

Formula	Gd(Cu, Ga) ₁₂	Tb(Cu, Ga) ₁₂	Dy(Cu, Ga) ₁₂	Ho(Cu, Ga) ₁₂	Er(Cu, Ga) ₁₂	Yb(Cu, Ga) ₁₂	Y(Cu, Ga) ₁₂
<i>a</i> (Å)	8.637(3)	8.622(3)	8.612(3)	8.600(3)	8.591(4)	8.650(3)	8.610(4)
<i>c</i> (Å)	5.175(2)	5.175(2)	5.171(2)	5.166(2)	5.163(3)	5.151(2)	5.172(2)
<i>V</i> (Å ³)	386.0(2)	384.7(2)	383.5(2)	382.1(2)	381.1(3)	385.4(2)	383.4(3)
<i>Z</i>	2	2	2	2	2	2	2
Crystal system	Tetragonal	Tetragonal	Tetragonal	Tetragonal	Tetragonal	Tetragonal	Tetragonal
Space group	<i>I4/mmm</i>	<i>I4/mmm</i>	<i>I4/mmm</i>	<i>I4/mmm</i>	<i>I4/mmm</i>	<i>I4/mmm</i>	<i>I4/mmm</i>
θ range (deg)	3.34–30.01	3.34–29.99	3.35–30.03	3.35–29.95	3.35–29.99	3.33–29.99	3.35–30.04
μ (mm ⁻¹)	46.534	47.268	47.936	48.692	49.452	50.139	45.81
Data collection:							
Measured reflections	482	450	475	467	466	458	442
Independent reflections	190	188	188	185	187	190	188
Reflections with $I > 2\sigma(I)$	182	183	180	180	179	183	184
R_{int}	0.0469	0.0422	0.0488	0.0363	0.0402	0.0557	0.0467
<i>h</i>	−12 → 12	−11 → 12	−11 → 12	−11 → 12	−11 → 12	−12 → 12	−11 → 12
<i>k</i>	−8 → 8	−8 → 8	−8 → 8	−8 → 8	−8 → 8	−8 → 8	−8 → 8
<i>l</i>	−7 → 5	−7 → 5	−7 → 5	−7 → 5	−6 → 7	−7 → 5	−7 → 5
Refinement:							
$R_1[F^2 > 2\sigma(F^2)]^a$	0.0277	0.0339	0.0244	0.0344	0.0279	0.0231	0.0265
$wR_2(F^2)^b$	0.0651	0.0788	0.0599	0.0916	0.0638	0.0574	0.058
Reflections	190	188	188	185	187	190	188
Parameters	16	16	16	16	16	16	16
$\Delta\rho_{\text{max}}$ (e Å ⁻³)	2.992	1.752	1.975	2.706	1.532	1.107	1.611
$\Delta\rho_{\text{min}}$ (e Å ⁻³)	−1.869	−2.329	−1.06	−2.978	−1.591	−1.847	−1.179

$$^a R_1 = \sum |F_o| - |F_c| / \sum |F_o|.$$

$$^b wR_2 = [\sum [w(F_o^2 - F_c^2)] / \sum [w(F_o^2)^2]]^{1/2}. w = 1/[\sigma^2(F_o^2) + (0.0137P)^2 + 2.7483P], w = 1/[\sigma^2(F_o^2) + (0.00068P)^2 + 2.9974P],$$

$$w = 1/[\sigma^2(F_o^2) + (0.0192P)^2 + 10.2277P], w = 1/[\sigma^2(F_o^2) + (0.0000P)^2 + 7.1821P], w = 1/[\sigma^2(F_o^2) + (0.0339P)^2 + 14.2257P],$$

$$w = 1/[\sigma^2(F_o^2) + (0.0000P)^2 + 13.2723P], w = 1/[\sigma^2(F_o^2) + (0.0000P)^2 + 4.6790P], \text{ for Y, Gd–Er, and Yb, respectively.}$$

Table 2a. Selected interatomic distances for Ln(Cu, Al)₁₂ (Å). (Note: M0 = Al or Cu.)

	Ce(Cu, Al) ₁₂	Pr(Cu, Al) ₁₂	Sm(Cu, Al) ₁₂	Yb(Cu, Al) ₁₂	Y(Cu, Al) ₁₂
Ln environment:					
Ln1–Al1(x8)	3.073(2)	3.062(2)	3.0384(2)	3.016(2)	3.020(2)
Ln1–M0(x8)	3.2427(10)	3.2352(10)	3.2201(11)	3.2017(14)	3.2040(10)
Ln1–Cu1(x4)	3.3723(10)	3.3651(10)	3.3501(5)	3.3383(7)	3.3340(10)
Cu environment:					
Cu1–Cu1(x2)	2.5800(10)	2.5780(10)	2.5730(10)	2.5590(10)	2.5655(10)
Cu1–Al1(x4)	2.6972(7)	2.6906(7)	2.6765(7)	2.6626(10)	2.6632(7)
Cu1–M0(x4)	2.5643(2)	2.5597(2)	2.5499(5)	2.5409(7)	2.5389(2)

Table 2b. Selected interatomic distances Ln(Cu, Ga)₁₂ (Å). (Note: M1 and M2 = Cu or Ga.)

	Y(Cu, Ga) ₁₂	Gd(Cu, Ga) ₁₂	Tb(Cu, Ga) ₁₂	Dy(Cu, Ga) ₁₂	Ho(Cu, Ga) ₁₂	Er(Cu, Ga) ₁₂	Yb(Cu, Ga) ₁₂
Ln environment:							
Ln–M1(x8)	2.9916(16)	3.0036(15)	2.9947(18)	2.9890(15)	2.983(2)	2.978(2)	2.9961(15)
Ln–M2(x8)	3.1766(11)	3.1856(12)	3.1814(14)	3.1756(12)	3.1712(15)	3.1661(17)	3.1767(12)
Ln–Cu(x4)	3.3073(13)	3.3164(10)	3.3115(10)	3.3079(10)	3.3035(10)	3.3003(13)	3.3183(10)
Cu environment:							
Cu–Cu(x2)	2.5860(10)	2.5875(10)	2.5875(10)	2.5855(10)	2.5830(10)	2.5815(15)	2.5755(10)
Cu–M1(x4)	2.6475(10)	2.6550(8)	2.6503(9)	2.6468(8)	2.6428(9)	2.6397(11)	2.6514(8)
Cu–M2(x4)	2.5298(9)	2.5351(7)	2.5323(7)	2.5303(7)	2.5272(7)	2.5255(10)	2.5350(7)

probe microanalysis was performed using a JEOL JSM-5060 scanning electron microscope equipped with an energy dispersive spectrometer. The accelerating voltage was 15 kV with a beam to sample distance of 20 mm. An average of 5–7 scans were performed on each single crystal. The results are provided in table 4. After taking account of elemental analysis results, the structures of Ln(Cu, Al)₁₂ and Ln(Cu, Ga)₁₂ were carefully checked for mixed occupancy on all Cu and Al/Ga sites, and refinements of single-crystal x-ray diffraction data suggest that the 8j site in Ln(Cu, Al)₁₂ and the 8i and 8j sites in Ln(Cu, Ga)₁₂ are occupied statistically by Cu and Al or Ga respectively (8i will be denoted as Al1 or M1 (M1 has joint occupancy of Cu and Ga) whereas 8j will be denoted as M0 and M2 where Cu/Al and Cu/Ga jointly occupy this position, respectively). The structural models showed stoichiometry for Ln:Cu:Al and Ln:Cu:Ga similar to the result from elemental analysis. For simplicity, we will discuss the compounds as Ln(Cu, Al)₁₂ or Ln(Cu, Ga)₁₂ where (Ln = Y, Ce, Pr, Sm, and Yb for Al and Ln = Y, Gd–Er, Yb for Ga).

For all growths, ground single-crystal samples were characterized using x-ray powder diffraction to confirm phase purity with a Bruker AXS D8 advance diffractometer.

2.3. Physical properties

Magnetic data were collected using a Quantum Design Physical Property Measurement System (PPMS). The temperature-dependent susceptibility data were measured under zero-field-cooled (ZFC) conditions from 2–3 to 285–300 K under an applied field of 0.1 T for Al and Ga compounds, and then measured upon heating to obtain field-cooled (FC) data after cooling to 2 K under a field for Ga. Field-dependent magnetization data were measured at 3 K with field up to 9 T. The electrical resistivity and magnetoresistance (MR) were

measured by the standard four-probe AC technique. The heat capacity was measured by the standard adiabatic heat pulse relaxation technique down to 0.4 K.

3. Results and discussion

3.1. Structure

The ThMn₁₂ structure type has been well studied and has been shown to crystallize with a general formula of Ln(TM, X)₁₂; Ln = rare earth, TM = transition metal, X = main group element [15]. Herein, Ce(Cu, Al)₁₂ will be discussed as a general structural model for the series of rare earth aluminides and gallides reported in this work, as only unit cell parameters such as the *a* or *c* unit cell lengths change due to lanthanide contraction. This pseudo-binary crystallizes in the tetragonal *I4/mmm* space group with the Ln, Cu, (Al or M1) and M0 or M2 (M0(8j)–Cu/Al, M1(8i)–Cu/Ga, and M2(8j)–Cu/Ga mixing) occupying 2a, 8f, 8i, and 8j sites respectively. It was found that statistical disorder is observed on the 8j site for Al containing compounds and the 8i and 8j sites for Ga analogues. The degree of statistical disorder depends on the reaction ratio, dwell times, and the lanthanide.

Figure 1(a) illustrates the Ln (Ln = Ce–Nd, Sm, Gd–Yb) polyhedral environment; each polyhedron is comprised of eight Cu atoms (medium yellow spheres), four Al atoms (small green spheres, identified as M1 in Ga analogues), and eight M0 atoms (small purple spheres, identified as M2 in Ga analogues). The Ce environment is similar to that of SmCu₄Ga₈ (hexagonal), which belongs to the family of CaCu₅ structure type. M0 atoms are face sharing atoms in the polyhedron around the Ce atom (large powder blue spheres), in which the Ce polyhedra are corner sharing through Cu atoms. The polyhedron is comprised of two perpendicular six-member rings which are

Table 3a. Atomic positions and thermal parameters for Ln(Cu, Al)₁₂. (Note: M0 = Cu and Al.)

Atom	Wyckoff position	x	y	z	U_{eq} (Å ²) ^a
Ce	2a	0	0	0	0.0048(4)
Cu	8f	1/4	1/4	1/4	0.0091(4)
Al	8i	0.348 3(3)	0	0	0.0059(8)
M0	8j	0.277 1(2)	1/2	0	0.0135(10)
Pr	2a	0	0	0	0.0026(3)
Cu	8f	1/4	1/4	1/4	0.0067(4)
Al	8i	0.348 3(2)	0	0	0.0052(8)
M0	8j	0.277 69(18)	1/2	0	0.0105(9)
Sm	2a	0	0	0	0.0043(3)
Cu	8f	1/4	1/4	1/4	0.0085(3)
Al	8i	0.347 29(18)	0	0	0.0064(7)
M0	8j	0.278 70(14)	1/2	0	0.0156(7)
Yb	2a	0	0	0	0.0030(3)
Cu	8f	1/4	1/4	1/4	0.0064(4)
Al	8i	0.345 8(3)	0	0	0.0048(9)
M0	8j	0.279 4(2)	1/2	0	0.0144(10)
Y	2a	0	0	0	0.0057(5)
Cu	8f	1/4	1/4	1/4	0.0097(5)
Al	8i	0.347 0(3)	0	0	0.0070(11)
M0	8j	0.279 5(2)	1/2	0.00	0.0165(9)

^a U_{eq} is defined as a third of the trace of the orthogonalized U_{ij} tensor.

coordinated about the Ce atom. Each ring is composed of two Al and four M0 atoms. The rectangular prism of Cu atoms is situated such that two Cu positions are set at $\sim 45^\circ$ between the two perpendicular six-member rings, essentially bi-capping the structure as shown in the figure 1(b). The face sharing 8j sites are the locations of mixing in the ternary phase. These sites (tables 3a and 3b), whose bond distances are listed in tables 2a and 2b, show that this M0 position is at an intermediate distance when compared to the Cu and Al bond lengths, giving rise to the potential for statistical disorder on this 8j site.

Figures 2(a) and (b) show the structural relationship between ThMn₁₂ and CaCu₅ structure types [30] (hereafter, ThMn₁₂ and CaCu₅ are represented as RT₁₂ and RT₅, respectively for clarity). The relationship of the lattice parameters has previously been described as the following: $aRT_{12} \approx \sqrt{3}aRT_5 \approx 2cRT_5$; $cRT_{12} \approx aRT_5 \approx aRT_{12}/\sqrt{3}$ [31, 32]. The transformation from RT₅ to RT₁₂ structure is caused by systematic substitution of a pair of T atoms for R atoms along the *c*-axis from the parental RT₅ structure. This can be described using the equation $2(RT_5) - R + 2T$ (a pair of Ts) \rightarrow RT₁₂ [33, 34]. The crystallographic sites between the hexagonal $P6/mmm$ RT₅ and tetragonal $I4/mmm$ RT₁₂ are shown in figures 2(a)–(c).

3.2. Physical properties

3.2.1. Ln(Cu, Al)₁₂. Figures 3–5 show the temperature dependence of the magnetic susceptibility of single crystals of Ln(Cu, Al)₁₂ (Ln = Ce, Pr, Sm) measured at an applied field of 0.1 T and the field dependence of the magnetization at 3 K. The magnetic susceptibility for all three compounds

Table 3b. Atomic positions and thermal parameters for Ln(Cu, Ga)₁₂. (Note: M1 and M2 = Cu and Ga.)

Atom	Wyckoff position	x	y	z	U_{eq} (Å ²) ^a
Y	2a	0	0	0	0.0042(4)
Cu	8f	1/4	1/4	1/4	0.0078(3)
M1	8i	0.347 46(9)	0	0	0.0097(3)
M2	8j	0.285 74(12)	1/2	0	0.0140(3)
Gd	2a	0	0	0	0.0065(3)
Cu	8f	1/4	1/4	1/4	0.0096(4)
M1	8i	0.347 76(12)	0	0	0.0121(4)
M2	8j	0.284 86(16)	1/2	0	0.0161(4)
Tb	2a	0	0	0	0.0058(4)
Cu	8f	1/4	1/4	1/4	0.0089(5)
M1	8i	0.347 34(17)	0	0	0.0113(4)
M2	8j	0.285 3(2)	1/2	0	0.0161(5)
Dy	2a	0	0	0	0.0054(3)
Cu	8f	1/4	1/4	1/4	0.0089(4)
M1	8i	0.347 07(13)	0	0	0.0108(4)
M2	8j	0.285 90(17)	1/2	0	0.0158(4)
Ho	2a	0	0	0	0.0026(5)
Cu	8f	1/4	1/4	1/4	0.0060(5)
M1	8i	0.346 84(19)	0	0	0.0079(5)
M2	8j	0.286 1(2)	1/2	0	0.0132(5)
Er	2a	0	0	0	0.0028(4)
Cu	8f	1/4	1/4	1/4	0.0061(4)
M1	8i	0.346 64(17)	0	0	0.0076(4)
M2	8j	0.286 6(2)	1/2	0	0.0139(5)
Yb	2a	0	0	0	0.0048(3)
Cu	8f	1/4	1/4	1/4	0.0076(3)
M1	8i	0.346 38(12)	0	0	0.0089(3)
M2	8j	0.285 02(16)	1/2	0	0.0157(4)

^a U_{eq} is defined as a third of the trace of the orthogonalized U_{ij} tensor.

was fitted to a Curie–Weiss equation of the following form: $\chi(T) = \chi_0 + C/(T - \theta)$, where C represents the Curie constant and θ is the Weiss temperature in the paramagnetic state, and where χ_0 is a constant positive background. The effective moments obtained from C were compared to the calculated values using $\mu_{eff} = g_J(J(J+1))^{1/2}$; they are both summarized in table 5.

The temperature-dependent magnetic susceptibility of Ce(Cu, Al)₁₂ in an applied field of 0.1 T is shown in figure 3(a). The material is paramagnetic down to 3 K with no magnetic transition. The effective moment (35–253 K) of the Ce³⁺ ion was determined as 2.63 μ_B which is close the calculated effective moment of 2.54 μ_B . A negative Weiss constant, $\theta = -106.6$ K, indicates strong antiferromagnetic correlations. The field-dependent magnetization is presented in figure 3(b) for Ce(Cu, Al)₁₂ at 3 K and shows no saturation up to 9 T.

Figure 4(a) shows the temperature-dependent magnetic susceptibility of Pr(Cu, Al)₁₂, measured with the magnetic field of 0.1 T parallel to the *c*-axis ($H \parallel c$) and perpendicular to it ($H \parallel ab$). Pr(Cu, Al)₁₂, like the Ce analogue, is paramagnetic down to 3 K for both field orientations. The effective moment determined from the Curie–Weiss equation for the Pr³⁺ ion (20–200 K) was found to be 3.26 μ_B for $H \parallel ab$ and 3.78 μ_B for $H \parallel c$. Both values agree well with the calculated effective moment for Pr³⁺ of 3.54 μ_B . The Weiss

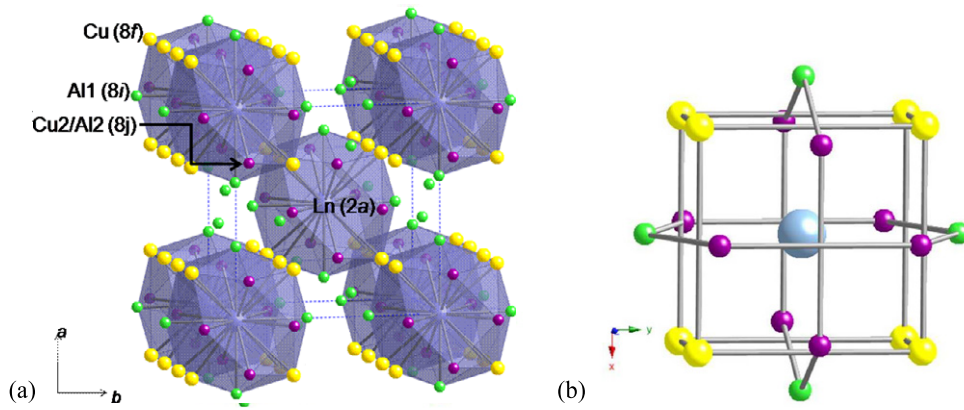


Figure 1. The crystal structure of $\text{Ce}(\text{Cu}, \text{Al})_{12}$ is shown in (a), where the Ce (2a) atoms are represented with large metallic blue spheres; Cu (8f) atoms are denoted as medium yellow spheres, Al (8i) atoms are denoted with small green spheres, and the M0 (8j) position is denoted with small purple spheres. Dashed lines are used to show the unit cell. The local (b) Ce environment is shown depicting the two perpendicular six-member rings with the square prismatic array of Cu atoms.

(This figure is in colour only in the electronic version)

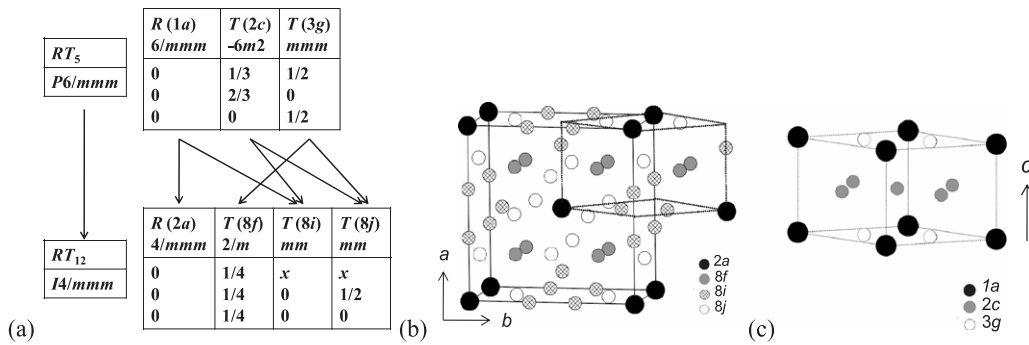


Figure 2. (a) The relationship between RT_{12} and RT_5 as adapted from [34]. The unit cell of (b) RT_{12} , in which the RT_5 unit cell is marked by solid lines. The original (c) unit cell of RT_5 is shown for comparison.

Table 4. Composition as obtained from electron probe microanalysis.

	$\text{Ce}(\text{Cu}, \text{Al})_{12}$	$\text{Pr}(\text{Cu}, \text{Al})_{12}$	$\text{Sm}(\text{Cu}, \text{Al})_{12}$	$\text{Yb}(\text{Cu}, \text{Al})_{12}$			
(Cu:Al) composition ^a	4.46(4):7.54(4)	4.65(4):7.35(4)	4.75(5):7.25(5)	4.77(8):7.23(8)			
	$\text{Y}(\text{Cu}, \text{Ga})_{12}$	$\text{Gd}(\text{Cu}, \text{Ga})_{12}$	$\text{Tb}(\text{Cu}, \text{Ga})_{12}$	$\text{Dy}(\text{Cu}, \text{Ga})_{12}$	$\text{Ho}(\text{Cu}, \text{Ga})_{12}$	$\text{Er}(\text{Cu}, \text{Ga})_{12}$	$\text{Yb}(\text{Cu}, \text{Ga})_{12}$
(Cu:Ga) composition ^a	5.63(11):6.37(11)	5.58(4):6.42(4)	5.53(11):6.47(11)	5.60(8):6.40(8)	5.67(13):6.33(13)	5.66(10):6.34(10)	5.36(10):6.64(10)

^a Composition is normalized to lanthanide.

Table 5. Magnetic properties of $\text{Ln}(\text{Cu}, \text{Al})_{12}$ (Ln = Y, Ce, Pr, Sm, and Yb).

	C	θ	$\mu_{\text{calc}} (\mu_B)$	$\mu_{\text{eff}} (\mu_B)$	Fit range (K)	The de Gennes factor [[$(g - 1)^2 J(J + 1)$]]	Ordering T_N (K)
$\text{Y}(\text{Cu}, \text{Al})_{12}$	—	—	—	—	—	—	PPM ^a
$\text{Ce}(\text{Cu}, \text{Al})_{12}$	0.869	-106.6	2.49	2.63	35–253	0.18	PM ^b
$\text{Pr}(\text{Cu}, \text{Al})_{12}$	1.786	-49.9	3.54	3.78	20–200	0.80	PM ($H \parallel c$)
	1.333	-36.4	3.54	3.26	20–200	—	PM ($H \parallel ab$)
$\text{Sm}(\text{Cu}, \text{Al})_{12}$	0.082	-26.7	0.71	0.81	10–300	4.46	AFM ^c 4.8
$\text{Yb}(\text{Cu}, \text{Al})_{12}$	—	—	—	—	—	—	PPM

^a Pauli paramagnetic. ^b Paramagnetic. ^c Antiferromagnetic.

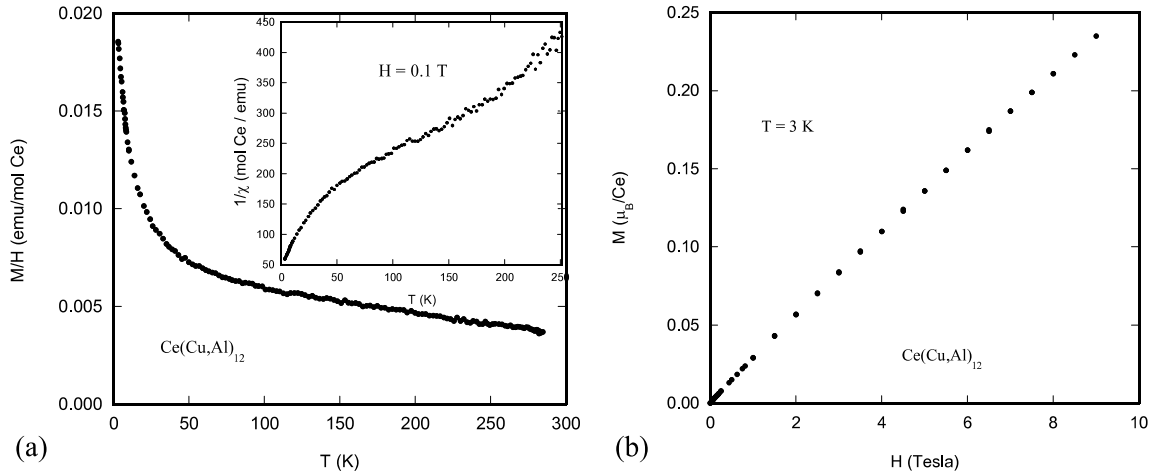


Figure 3. (a) Magnetic susceptibility (emu/mol Ce) of Ce(Cu, Al)₁₂ versus temperature. The inset shows the inverse magnetic susceptibility. (b) Magnetization of Ce(Cu, Al)₁₂ as a function of field at 3 K.

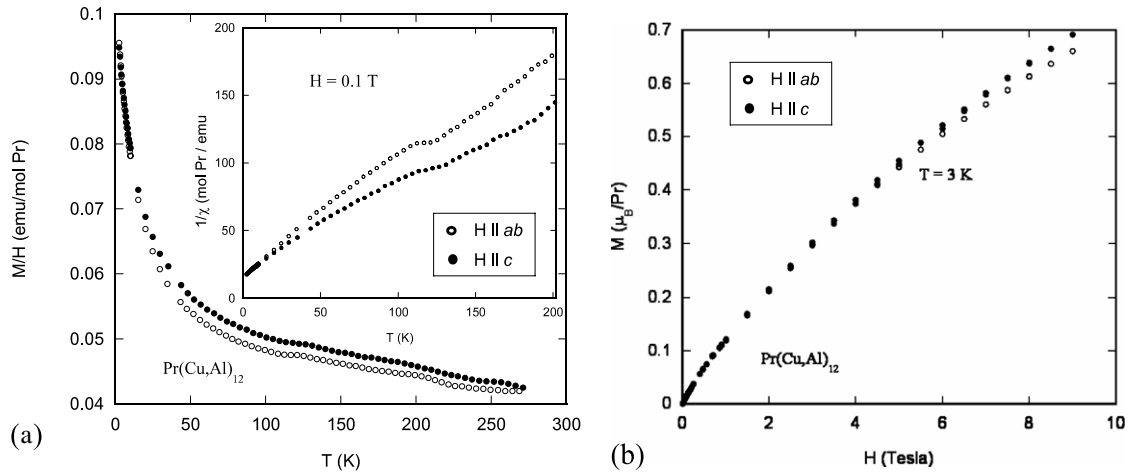


Figure 4. (a) Magnetic susceptibility (emu/mol Pr) of Pr(Cu, Al)₁₂ as a function of temperature is shown. The inset shows the inverse magnetic susceptibility. (b) Magnetization of Pr(Cu, Al)₁₂ as a function of field.

temperature for Pr(Cu, Al)₁₂ was found to be $\theta = -36.5$ K and -49.9 K for $H \parallel ab$ and $H \parallel c$, respectively, indicating weakly anisotropic antiferromagnetic interactions. The smaller value of θ in Pr(Cu, Al)₁₂, as compared to the Ce analogue, also implies weaker antiferromagnetic coupling. Figure 4(b) shows the field-dependent magnetization at 3 K in both the $H \parallel ab$ and $H \parallel c$ directions. A downward curvature is observed at ~ 2 T, and more dramatically for $H \parallel ab$, yet no saturation is observed up to 9 T, supporting the negative values of the Weiss constant.

The temperature-dependent magnetic susceptibility of Sm(Cu, Al)₁₂ is shown in figure 5(a), in an applied field of 0.1 T. Sm(Cu, Al)₁₂ has an antiferromagnetic transition at $T_N \sim 5$ K. The effective moment for the Sm³⁺ ion above 10 K, from the Curie–Weiss equation, was found to be $0.81 \mu_B$ which is close to the calculated effective moment of $0.71 \mu_B$. The Weiss temperature for Sm(Cu, Al)₁₂ was found to be $\theta = -26.7$ K. It is worth noting that the inverse susceptibility remains linear down to 10 K which is unusual for a Sm analogue. Deviations from Curie–Weiss behaviour in Sm compounds are generally attributed to Van Vleck

paramagnetism. The absence of a Van Vleck contribution in Sm(Cu, Al)₁₂ is probably due to the spherical environment of Sm³⁺ which minimizes the crystal electric field splitting. Figure 5(b) shows the field-dependent magnetization at 3 K. The magnetization is linear with no sign of saturation in the field measured, up to 9 T, as expected for an antiferromagnetic material.

The Curie–Weiss parameters and the observed and calculated effective moment values are summarized in table 5. These findings are in contrast to some previous reports which show PrCu₄Al₈ and SmCu₄Al₈ to order antiferromagnetically with $T_N \simeq 15$ and $\simeq 25$ K [19]. Multiple attempts to grow these materials stoichiometrically were unsuccessful. It is still unclear what the source was for the 15 and 25 K Néel temperatures previously reported for the powder samples as the magnetic susceptibility, magnetization, resistivity, magnetoresistance, and heat capacity of single crystals measured here with the magnetic susceptibility for Pr(Cu, Al)₁₂ measured with $H \parallel c$ and $H \parallel ab$ showed no ordering down to 3 K and little magnetic anisotropy.

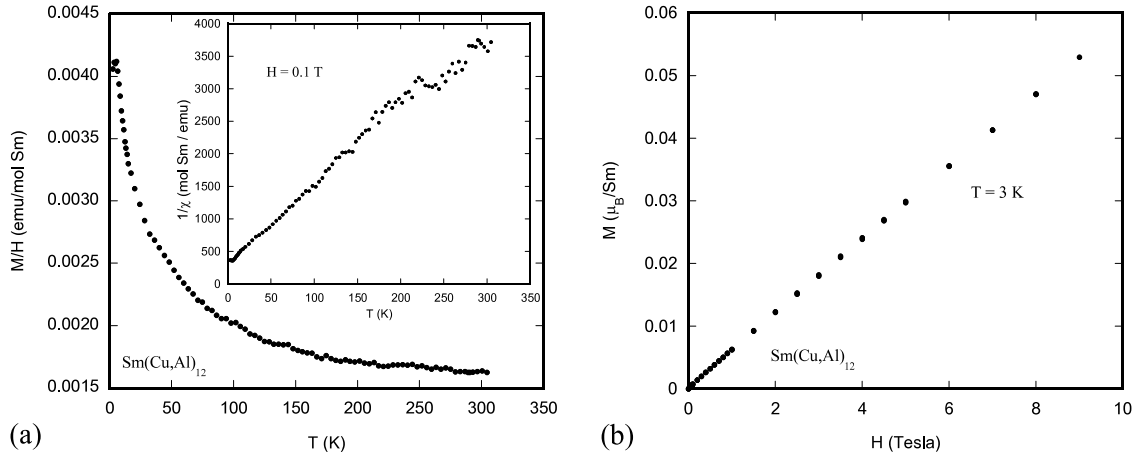


Figure 5. (a) Magnetic susceptibility (emu/mol Sm) of $\text{Sm}(\text{Cu}, \text{Al})_{12}$ as a function of temperature is shown. The inset shows the inverse magnetic susceptibility. (b) Magnetization of $\text{Sm}(\text{Cu}, \text{Al})_{12}$ as a function of field.

The magnetic susceptibility is positive for both $\text{Y}(\text{Cu}, \text{Al})_{12}$ and $\text{Yb}(\text{Cu}, \text{Al})_{12}$ and temperature independent, which we attribute to Pauli paramagnetism (not shown). The magnitude of $\chi_0 = 2.9 \times 10^{-3} \text{ emu mol}^{-1}$ found for $\text{Yb}(\text{Cu}, \text{Al})_{12}$ is consistent with the Pauli susceptibility, $\chi_{\text{PPM}} = 1.092 \times 10^{-3} \text{ emu mol}^{-1}$, determined from the experimental electronic specific heat coefficient $\gamma_0 = 11 \text{ mJ K}^{-2} \text{ mol}^{-1}$, using the Wilson ratio $R = (\pi^2 k_B^2 / g^2 J(J+1) \mu_B^2) \chi_{\text{PPM}} / \gamma_0 = 1$. It is also close to the values of $\chi_0 = 1.79 \times 10^{-3}$ and $1.36 \times 10^{-3} \text{ emu mol}^{-1}$ obtained for the Ce and Sm analogues respectively. The absence of Curie–Weiss behaviour in $\text{Yb}(\text{Cu}, \text{Al})_{12}$ is a strong indication that the valence of Yb is close to $2+$, a conclusion also supported by the analysis of the lattice volume evolution across the Ln series. As can be seen in table 1a, the $\text{Yb}(\text{Cu}, \text{Al})_{12}$ analogue shows a deviation from a Yb^{3+} ion in the lanthanide contraction indicating at least partial occupancy of Yb^{2+} . One would expect for a full occupation of the Yb^{2+} ion that the volume of the unit cell would be similar to that of a Sm^{3+} ion. With the existence of Yb^{2+} ions in the crystal lattice this effectively acts to magnetically dilute the system such that the Pauli paramagnetism is observed.

The electrical resistivities as a function of temperature for single crystals of $\text{Ln}(\text{Cu}, \text{Al})_{12}$ (Ln = Ce, Pr, Sm, Yb, and Y) are shown in figure 6. These compounds show metallic behaviour with residual resistivity ratio (RRR) values of 3.0, 1.6, 1.6, 2.1, and 1.5 for Ce, Pr, Sm, Yb, and Y analogues, respectively. For Pr, Yb, and Y no anomalous behaviour is observed. $\text{Ce}(\text{Cu}, \text{Al})_{12}$ shows deviations from an expected linear resistivity which may be attributed to some Kondo-like behaviour from the screening of conduction electrons. In figure 6 the inset is a blow-up of the low temperature data for $\text{Sm}(\text{Cu}, \text{Al})_{12}$. A small kink is observed at $\sim 5 \text{ K}$, coinciding with the AFM transition at $\sim 5 \text{ K}$ observed in the magnetic susceptibility data. The resistivity saturates below 5 K with no indication of a reduced spin disorder scattering.

Heat capacity data were collected for $\text{Ln}(\text{Cu}, \text{Al})_{12}$ where Ln = Ce, Pr, Sm, Yb, and Y. The $\text{Y}(\text{Cu}, \text{Al})_{12}$ analogue was used to subtract the phonon contribution to the heat capacity

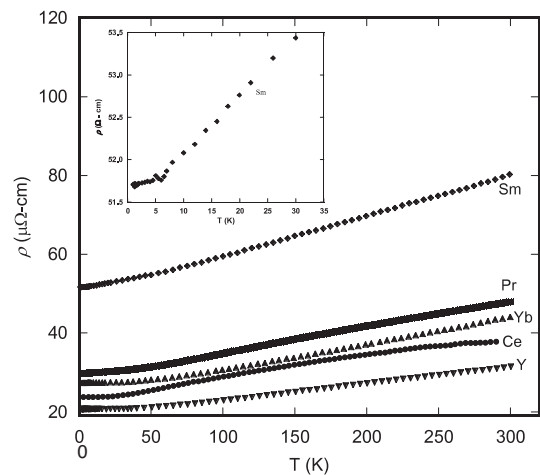


Figure 6. Normalized electrical resistivity of $\text{Ln}(\text{Cu}, \text{Al})_{12}$ (Ln = Ce, Pr, Sm, Yb, and Y) as a function of temperature is shown. The inset shows a blow-up of the low temperature resistivity of $\text{Sm}(\text{Cu}, \text{Al})_{12}$.

for the Ce, Pr, and Sm compounds. Attempts were made to grow the La derivative, but all synthesis attempts result in the formation of $\text{La}(\text{Cu}, \text{Al})_{13}$, a cubic phase with the NaZn_{13} structure. Figures 7(a) and (b) show the plots of C_p versus T and C_p/T versus T (inset: C_p/T versus T^2). In figure 7(b) the data provided have had the phonon contribution to the heat capacity, as determined for $\text{Y}(\text{Cu}, \text{Al})_{12}$, subtracted.

As is clear in figures 7(a) and (b), $\text{Ce}(\text{Cu}, \text{Al})_{12}$ shows a transition at $\sim 2 \text{ K}$. Magnetic susceptibility data were collected down to 3 K . From consideration of the negative θ_W value, it is thought that the transition in the heat capacity data is an antiferromagnetic ordering at $\sim 2 \text{ K}$. With the absence of antiferromagnetic ordering in the magnetic susceptibility data and the absence of an anomaly in the heat capacity, the previous report of $T_N = 5.8 \text{ K}$ is not supported by the single-crystal physical property measurements [21]. In addition, analysis of the low temperature portion of the heat

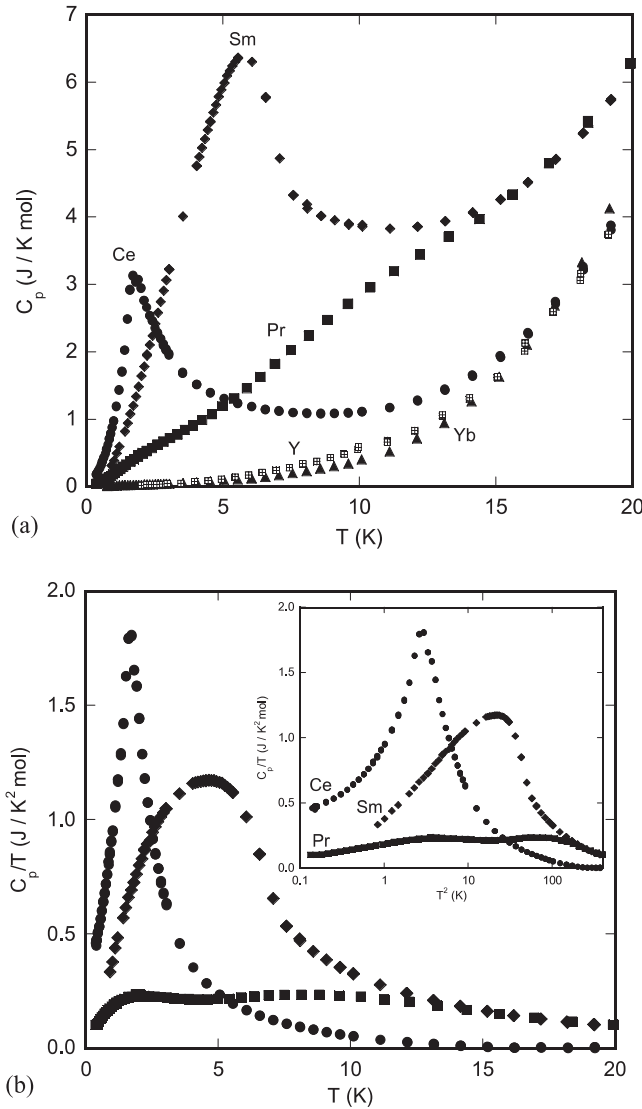


Figure 7. (a) Heat capacity versus temperature for $\text{Ln}(\text{Cu}, \text{Al})_{12}$ ($\text{Ln} = \text{Y}, \text{Ce}, \text{Pr}, \text{Sm},$ and Yb). (b) Electronic heat capacity C_p/T as a function of temperature; the inset shows C_p/T versus T^2 .

capacity shows that $\text{Ce}(\text{Cu}, \text{Al})_{12}$ is a heavy fermion, with a Sommerfeld coefficient, obtained from a linear fit of C_p/T versus T^2 for $T < 1$ K, of $\gamma \sim 390$ $\text{mJ K}^{-2}/\text{mol Ce}$, corresponding to a mass enhancement of 39 compared to the non-magnetic Yb analogue case. This is also supported by the fact that the entropy at 2 K is only $0.35R \ln 2$, the full magnetic entropy $S_{\text{mag}} = R \ln 2$ being recovered only at 20 K. The missing entropy is probably the result of the Kondo screening of the Ce^{3+} moments at low temperatures. The temperature dependence of the resistivity also suggests the presence of Kondo screening (see figure 6). The partial recovery of the magnetic entropy at 2 K reinforces the notion that the large γ value retrieved from the low temperature fit is a signature of a heavy fermion, which is in agreement with earlier reports [20–22].

Heat capacity data for $\text{Pr}(\text{Cu}, \text{Al})_{12}$ and $\text{Sm}(\text{Cu}, \text{Al})_{12}$ are also presented in figures 7(a) and (b). $\text{Pr}(\text{Cu}, \text{Al})_{12}$ shows two broad peaks in the low temperature range, $T_{\text{anom}} \sim 1.9$

and 8.8 K. A two-level Schottky formula does not give a satisfactory fit of the broad peak at 8.8 K. Nevertheless, this feature might correspond to a multi-level Schottky anomaly, since there is no indication of magnetic ordering in the susceptibility data at this temperature. For the second peak at the lower temperature, we cannot rule out the possibility of an antiferromagnetic transition, since the susceptibility has only been measured down to 3 K. From the fit of the linear low temperature regime of $\text{Pr}(\text{Cu}, \text{Al})_{12}$ heat capacity data, C_p/T versus T^2 for $T < 0.7$ K, a rather large electronic specific heat coefficient is obtained, $\gamma = \sim 80$ $\text{mJ K}^{-2}/\text{mol Pr}$. This value shows a mass enhancement of a factor of 8 as compared to the non-magnetic Yb analogue. For the Sm analogue, a broad peak can be seen in figures 7(a) and (b) at ~ 5 K, coinciding with the antiferromagnetic transition observed in the magnetic susceptibility data. In addition, fits of the low temperature regime of C_p yield $\gamma \sim 130$ $\text{mJ K}^{-2}/\text{mol Sm}$. Heat capacity data were collected only down to 0.9 K for this compound. The entropy recovered at 5 K is $R \ln 2$. It remains unclear whether this represents the full magnetic entropy, as one would expect $R \ln(2J + 1) = R \ln 6$ for Sm^{3+} in the absence of crystal field splitting. On the basis of the spherical environment and the absence of Van Vleck interactions, it could be asserted that the splitting is negligible and the entropy does follow $R \ln(2J + 1)$. Following this assumption, only 39% of the expected full magnetic entropy ($R \ln 6$) is recovered at the transition (with C/T integrated from 1 to 7 K), possibly due to the Kondo screening. It is unclear at this time whether $\text{Sm}(\text{Cu}, \text{Al})_{12}$ is a heavy electron system, or whether the Sommerfeld coefficient is large due to the transition.

3.2.2. $\text{Ln}(\text{Cu}, \text{Ga})_{12}$. Figures 10–14 show the temperature-dependent magnetic susceptibility of single crystals of $\text{Ln}(\text{Cu}, \text{Ga})_{12}$ ($\text{Ln} = \text{Gd–Er}$) measured at an applied field of 0.1 T along the crystallographic c -axis and ab -plane. The magnetic susceptibility of the compounds was fitted to a Curie–Weiss equation of the following form: $\chi(T) = C/(T - \theta)$, where C represents the Curie constant and θ is the Weiss temperature in the paramagnetic temperature ranges ($T > 50$ K). The effective moments were obtained from $\mu_{\text{eff}} = g_J(J(J + 1))^{1/2}$ and are summarized in table 6.

For $\text{Y}(\text{Cu}, \text{Ga})_{12}$ and $\text{Yb}(\text{Cu}, \text{Ga})_{12}$ the magnetic susceptibility is positive, but negligible without the temperature dependence, which is not shown here. This indicates that the ytterbium in $\text{Yb}(\text{Cu}, \text{Ga})_{12}$ is mixed valence, consistently with the Yb cell volume.

The temperature-dependent magnetization along the two crystallographic directions of $\text{Gd}(\text{Cu}, \text{Ga})_{12}$ is shown in figure 8(a) and is isotropic over the whole temperature range. This is consistent with the fact that Gd^{3+} has no orbital moment ($L = 0$), only spin. Therefore, the spin–orbit coupling is weak and there is no crystal field splitting for Gd^{3+} . The absence of magnetic anisotropy in the Gd sample, in contrast to all other lanthanides, may be due to the absence of crystal field splitting for Gd^{3+} . $\text{Gd}(\text{Cu}, \text{Ga})_{12}$ orders antiferromagnetically at 12.5 K for both directions. The effective moments of $8.35 \mu_B/\text{Gd}$ ($H \parallel c$) and $7.85 \mu_B/\text{Gd}$ ($H \parallel ab$) which are close to the calculated value of $7.94 \mu_B$ for Gd^{3+} were obtained

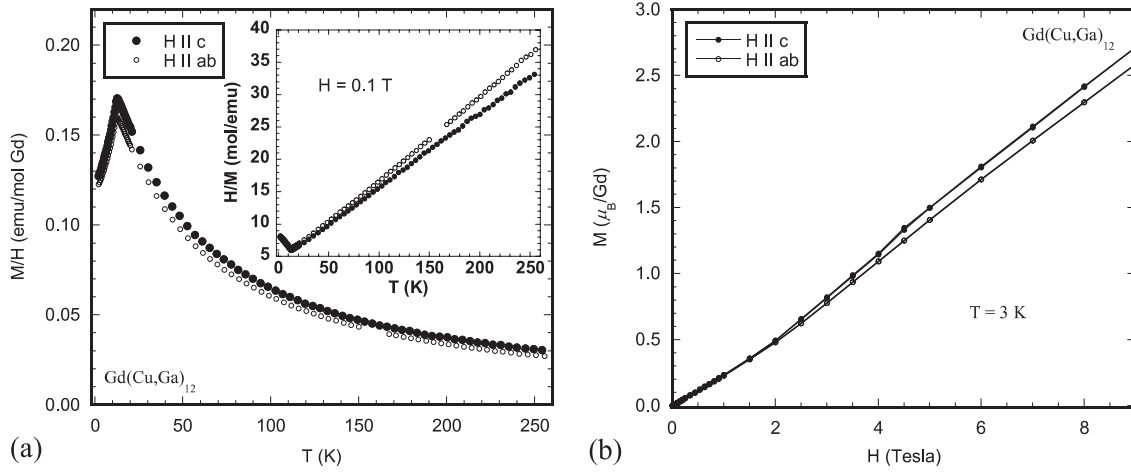


Figure 8. (a) Magnetic susceptibility (emu/mol Gd) of Gd(Cu, Ga)₁₂ as a function of temperature is shown. The inset shows the inverse magnetic susceptibility. (b) Magnetization of Gd(Cu, Ga)₁₂ as a function of field.

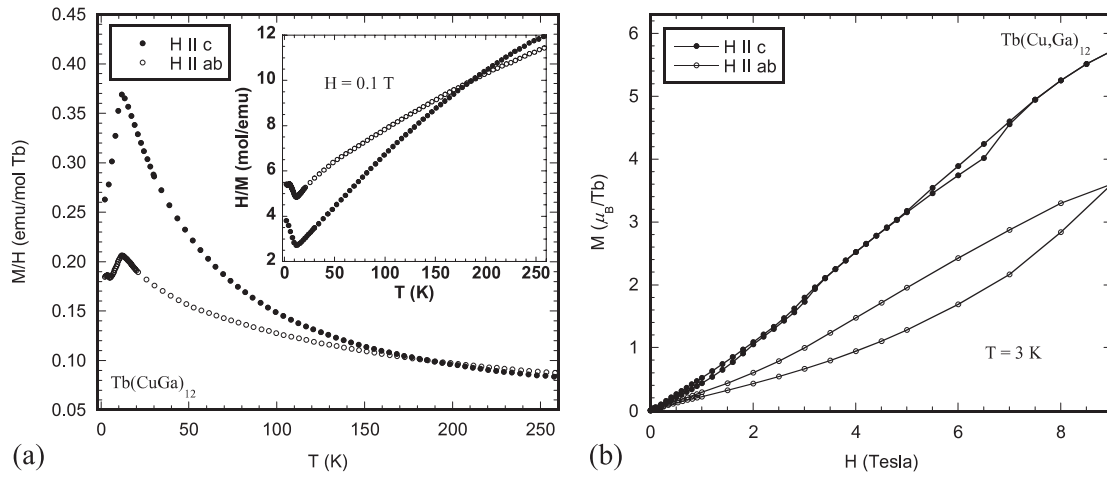


Figure 9. (a) Magnetic susceptibility (emu/mol Tb) of Tb(Cu, Ga)₁₂ as a function of temperature is shown. The inset shows the inverse magnetic susceptibility. (b) Magnetization of Tb(Cu, Ga)₁₂ as a function of field.

Table 6. Magnetic properties of Ln(Cu, Ga)₁₂ (Ln = Y, Gd–Er, Yb).

	C	θ	$\mu_{\text{calc}} (\mu_B)$	$\mu_{\text{eff}} (\mu_B)$	Fit range (K)	The de Gennes factor [[$(g-1)^2 J(J+1)$]]	Ordering T_N (K)
Y(Cu, Ga) ₁₂	—	—	—	—	—	—	PPM ^a
Gd(Cu, Ga) ₁₂	8.728	-36.32	7.94	8.35	50–260	15.75	AFM ^b 12.5 ($H \parallel c$) AFM 12.5 ($H \parallel ab$)
Tb(Cu, Ga) ₁₂	14.435	-23.45	9.72	10.74	50–260	10.5	AFM 13.5 ($H \parallel c$) AFM 13.5 ($H \parallel ab$)
Dy(Cu, Ga) ₁₂	14.74	-1.16	10.65	10.85	50–260	7.08	AFM 6.7 ($H \parallel c$) AFM 6.7 ($H \parallel ab$)
Ho(Cu, Ga) ₁₂	13.821	1.03	10.61	10.51	50–260	4.5	PM ^c ($H \parallel c$) PM ($H \parallel ab$)
Er(Cu, Ga) ₁₂	11.517	13.48	9.58	9.59	50–260	2.55	AFM 3.4 ($H \parallel c$) PM ($H \parallel ab$)
Yb(Cu, Ga) ₁₂	—	—	—	—	—	—	PPM

^a Pauli paramagnetic. ^b Antiferromagnetic. ^c Paramagnetic.

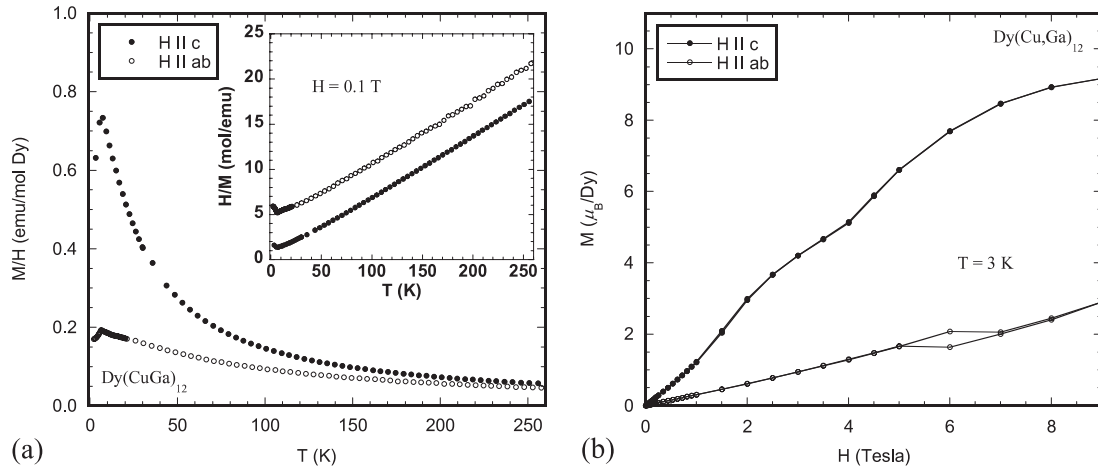


Figure 10. (a) Magnetic susceptibility (emu/mol Dy) of Dy(Cu, Ga)₁₂ as a function of temperature is shown. The inset shows the inverse magnetic susceptibility. (b) Magnetization of Dy(Cu, Ga)₁₂ as a function of field.

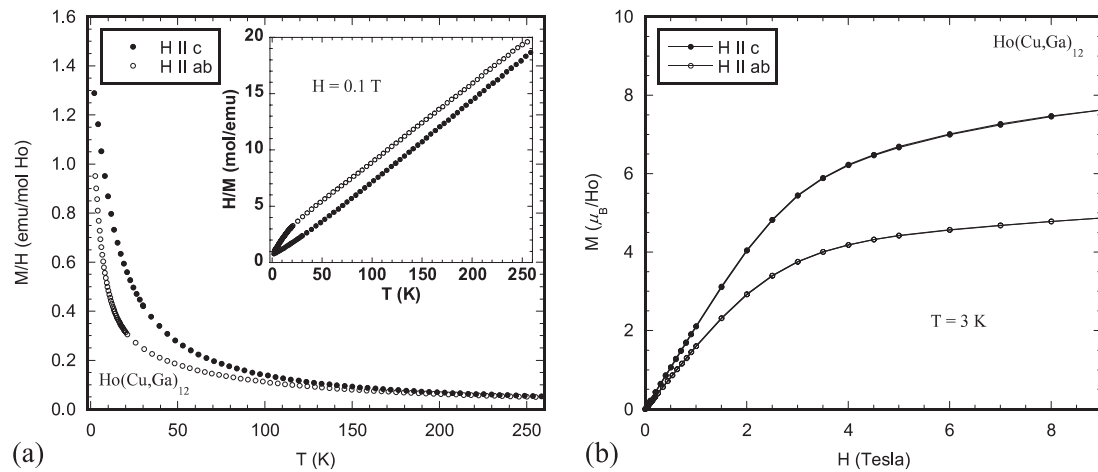


Figure 11. (a) Magnetic susceptibility (emu/mol Ho) of Ho(Cu, Ga)₁₂ as a function of temperature is shown. The inset shows the inverse magnetic susceptibility. (b) Magnetization of Ho(Cu, Ga)₁₂ as a function of field.

and the large negative Weiss constants, $\theta = -36.32$ and -28.42 K for the c -axis and ab -plane, respectively, indicate strong antiferromagnetic correlations in this compound. The field-dependent magnetization for Gd(Cu, Ga)₁₂ at 3 K is also isotropic with a metamagnetic transition at ~ 1.5 T for both directions as shown in figure 8(b). One would expect a lower ordering temperature due to a systematic substitution of a pair of T ($T = \text{Cu}$ or Ga in this case) atoms for magnetic Gd atoms in Gd(Cu, Ga)₁₂. In comparison GdCu₅ and GdCu₄Ga, which are isostructural to the RT₅ structure type, show antiferromagnetic transitions at 26 K with $\theta = 7$ K and 36 K with $\theta = -7.4$ K, respectively [35, 36].

Figure 9(a) shows the temperature-dependent magnetization for Tb(Cu, Ga)₁₂. A downturn at 13.5 K, which indicates antiferromagnetic ordering, is observed for both directions. Unlike for the Gd analogue, a clear anisotropic behaviour at low temperatures is shown in the temperature-dependent magnetization of Tb(Cu, Ga)₁₂. The magnetic susceptibility data for Tb(Cu, Ga)₁₂ can be fitted to a modified Curie–Weiss law in the following form: $\chi(T) = \chi_0 + C/(T - \theta)$, where χ_0 denotes the temperature-independent term, C represents the Curie constant and θ is the Weiss temperature giving effective

moments of $10.74 \mu_B/\text{Tb}$ ($H \parallel c$) and $10.96 \mu_B/\text{Tb}$ ($H \parallel ab$) which are close to the calculated value of $9.72 \mu_B$ for Tb^{3+} , and large negative Weiss constants, $\theta = -23.45$ K and -83.18 K for the c -axis and ab -plane, respectively, indicating strong antiferromagnetic correlations. The field-dependent magnetization for Tb(Cu, Ga)₁₂ at 3 K is also anisotropic and does not saturate up to 9 T for both directions (figure 9(b)).

An antiferromagnetic transition at 6.7 K in Dy(Cu, Ga)₁₂ is observed for both crystallographic directions (figure 10(a)). The temperature-dependent magnetization of Dy(Cu, Ga)₁₂ shows anisotropic behaviour. The data fit above 50 K yields effective moments of $10.85 \mu_B/\text{Dy}$ ($H \parallel c$) and $10.76 \mu_B/\text{Dy}$ ($H \parallel ab$) which are close to the expected value of $10.65 \mu_B$ for Dy^{3+} , and negative Weiss constants, $\theta = -1.16$ K and -53.97 K for the c -axis and ab -plane, respectively, consistent with antiferromagnetic ordering. Figure 10(b) shows the field-dependent isothermal magnetization of Dy(Cu, Ga)₁₂ at 3 K. The data show anisotropic behaviour and saturation along the c -axis.

Figure 11(a) shows the temperature-dependent magnetic susceptibility of Ho(Cu, Ga)₁₂, and no magnetic ordering is observed down to 2 K for both crystallographic directions. The

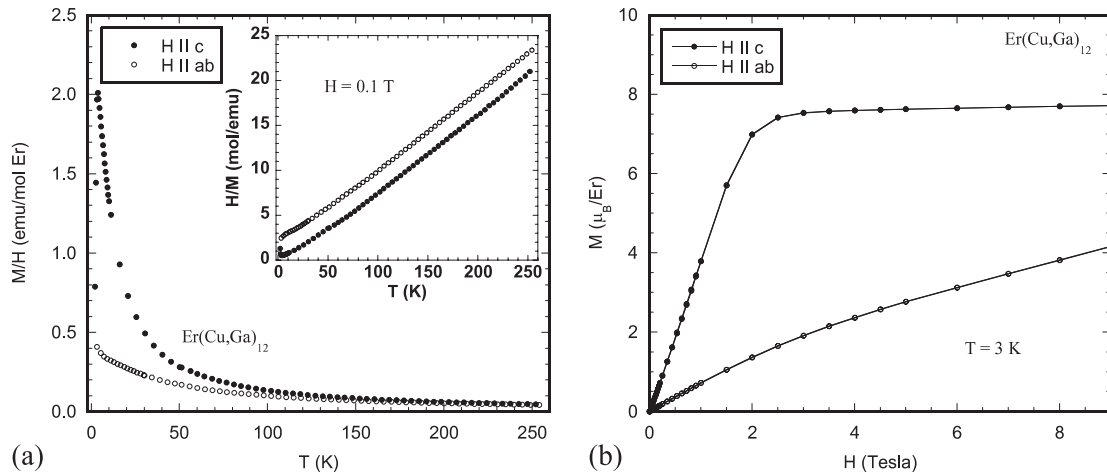


Figure 12. (a) Magnetic susceptibility (emu/mol Er) of Er(Cu, Ga)₁₂ as a function of temperature is shown. The inset shows the inverse magnetic susceptibility. (b) Magnetization of Er(Cu, Ga)₁₂ as a function of field.

data fit above 50 K gives effective moments of $10.51 \mu_B/\text{Ho}$ ($H \parallel c$) and $10.71 \mu_B/\text{Ho}$ ($H \parallel ab$) with large negative Weiss constant, $\theta = -28.17 \text{ K}$ along the ab -plane, indicating strong antiferromagnetic correlations. The field-dependent isothermal magnetization for Ho(Cu, Ga)₁₂ at 3 K is anisotropic and reaches the moments of $7.63 \mu_B/\text{Ho}$ ($H \parallel c$) and $4.88 \mu_B/\text{Ho}$ ($H \parallel ab$), respectively (figure 11(b)).

Highly anisotropic behaviour of the magnetic susceptibility for Er(Cu, Ga)₁₂ crystal is shown in figure 12(a). Er(Cu, Ga)₁₂ shows an antiferromagnetic transition at 3.4 K along the c -axis; however no magnetic ordering along the ab -plane is observed down to 2 K. Effective moments of $9.59 \mu_B/\text{Er}$ ($H \parallel c$) and $9.60 \mu_B/\text{Er}$ ($H \parallel ab$) and Weiss constants, $\theta = 13.48 \text{ K}$ and -15.16 K for the c -axis and ab -plane, respectively, are obtained by using a modified Curie–Weiss fit for the paramagnetic temperature range ($>50 \text{ K}$). The field-dependent magnetization for Er(Cu, Ga)₁₂ at 3 K also shows anisotropic behaviour consistent with magnetic susceptibility data. The magnetization of Er(Cu, Ga)₁₂ along the c -axis, which is an easy axis, saturates at 3 K since the easy axis is easily polarized (f electrons) under magnetic field (figure 12(b)).

The electrical resistivities as a function of temperature for single crystals of Ln(Cu, Ga)₁₂ (Ln = Y, Gd–Er, Yb) are shown in figure 13. These compounds show metallic behaviour with residual resistivity ratio (RRR) values of 4.1, 5.2, 2.3, 4.9, 3.1, 2.5, and 1.9 for Y, Gd, Tb, Dy, Ho, Er, and Yb analogues, respectively. The inset of figure 13 shows a blow-up of the low temperature resistivity data. There is no indication of a kink or any anomaly at their magnetic transition corresponding to the reduction of spin disorder scattering, which is highly unusual. One possibility is that the scattering of conduction electrons by $4f$ local moments is very anisotropic and the current is applied in the ab -plane which is not the easy axis of magnetization for Tb, Dy, and Er. On the other hand, the downturn in the temperature dependence of the resistivity around 30 K may reflect the spin disorder scattering.

Figure 14(a) shows the magnetoresistance ($\text{MR} = (\rho_H - \rho_0)/\rho_0 \times 100\%$) of single crystals of Ln(Cu, Ga)₁₂ (Ln = Y, Gd–Er) as a function of field at 3 K. Interestingly, large positive magnetoresistances of 117%, 127%, 28%, 150%,

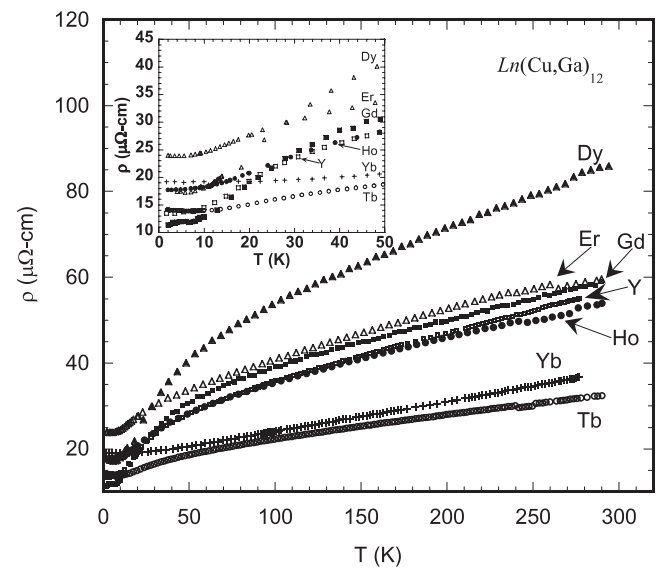


Figure 13. Normalized electrical resistivity of Ln(Cu, Ga)₁₂ (Ln = Y, Gd–Er, Yb) as a function of temperature is shown.

105%, and 141% are observed for Y, Gd, Tb, Dy, Ho, and Er analogues unlike the case for the RM₄Al₈ (R = Sc, Y, Ce, Yb, Lu; M = Cr, Mn, Fe) compounds which show negative magnetoresistance due to the Kondo-like interaction and spin glass state resulting from crystallographic disorder [5]. This positive magnetoresistance is also unusual, as most magnetic metals have negative magnetoresistance. Since the magnetic long-range interaction between the Ln moments is mediated by conduction electrons, one would expect spin disorder scattering to be suppressed below T_N or by applying magnetic field, resulting in a resistivity kink at T_N or/and negative magnetoresistance. Usually the strength of this coupling scales as the de Gennes factor as well (figure 14(b)). In Ln(Cu, Ga)₁₂ (Ln = Y, Gd–Er, Yb) this RKKY coupling seems to be either very anisotropic or anomalously small, resulting in a small negative contribution to the magnetoresistance. The observed positive, saturating magnetoresistance is probably classical magnetoresistance. Most interestingly, the magnetoresistance

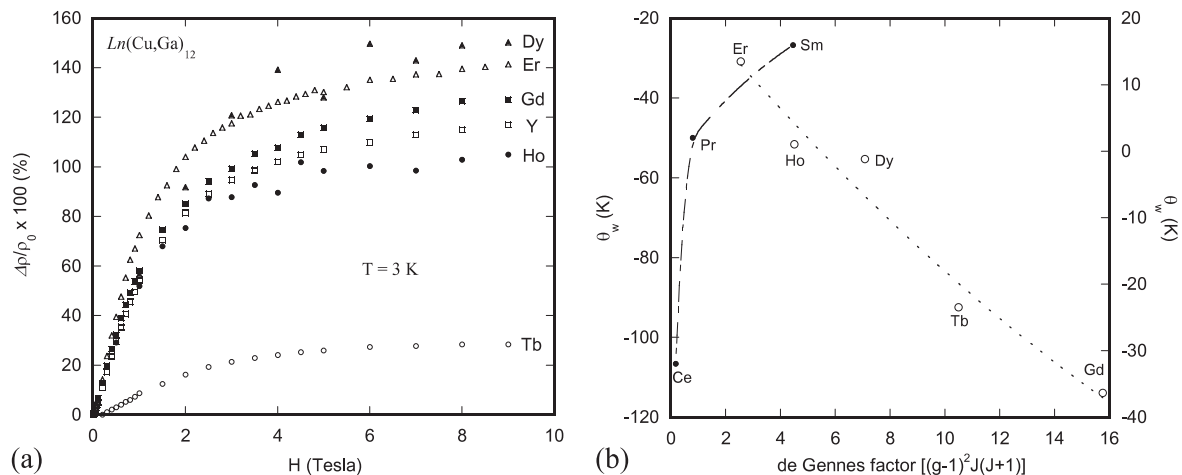


Figure 14. (a) MR% for $\text{Ln}(\text{Cu}, \text{Ga})_{12}$ ($\text{Ln} = \text{Y}, \text{Gd}-\text{Er}$) as a function of field at 3 K is shown. (b) Curie–Weiss temperature (K) as a function of the de Gennes factor. Closed circles correspond to $\text{Ln}(\text{Cu}, \text{Al})_{12}$ and open circles to $\text{Ln}(\text{Cu}, \text{Ga})_{12}$.

of $\text{Y}(\text{Cu}, \text{Ga})_{12}$ seems to behave like those of other magnetic analogues.

Overall, the Curie–Weiss temperatures obey the expected scaling as a function of the de Gennes factor $(g-1)^2 J(J+1)$ for $\text{Ln}(\text{Cu}, \text{Ga})_{12}$ analogues. In contrast, $\text{Ln}(\text{Cu}, \text{Al})_{12}$ does not scale with the de Gennes factor, which is attributed to frustration. The Ce analogue shows a large Weiss temperature of -106.6 K, whereas the T_N is only 2 K; the large difference between the two may be indicative of magnetic frustration or may be attributed to the Kondo effect. It is noteworthy that the two systems, $\text{Ln}(\text{Cu}, \text{Ga})_{12}$ and $\text{Ln}(\text{Cu}, \text{Al})_{12}$, despite being isoelectronic, and Al and Ga being in the same column of the periodic table, have very widely different magnetic properties.

In conclusion, we have reported structural and physical properties of single crystals of $\text{Ln}(\text{Cu}, \text{Al})_{12}$ ($\text{Ln} = \text{Y}, \text{Ce}, \text{Pr}, \text{Sm},$ and Yb) and $\text{Ln}(\text{Cu}, \text{Ga})_{12}$ ($\text{Ln} = \text{Y}, \text{Gd}-\text{Er}, \text{Yb}$) adopting the ThMn_{12} structure type. Crystallographic refinements of single-crystal x-ray diffraction data for $\text{Ln}(\text{Cu}, \text{Al})_{12}$ ($\text{Ln} = \text{Y}, \text{Ce}, \text{Pr}, \text{Sm},$ and Yb) suggest that the 8j site is occupied statistically by Cu and Al, and those for $\text{Ln}(\text{Cu}, \text{Ga})_{12}$ ($\text{Ln} = \text{Y}, \text{Gd}-\text{Er}, \text{Yb}$) suggest that 8i and 8j sites are occupied statistically by Cu and Ga. $\text{Ln}(\text{Cu}, \text{Al})_{12}$ ($\text{Ln} = \text{Sm}$) and $\text{Ln}(\text{Cu}, \text{Ga})_{12}$ ($\text{Ln} = \text{Gd}, \text{Tb}, \text{Dy},$ and Er) exhibit antiferromagnetic ordering at low temperatures. In addition, $\text{Ce}(\text{Cu}, \text{Al})_{12}$ shows heavy fermion characteristics, with $\text{Pr}(\text{Cu}, \text{Al})_{12}$ and $\text{Sm}(\text{Cu}, \text{Al})_{12}$ showing enhanced mass behaviour.

Acknowledgments

We acknowledge Ilya Vehkter for meaningful discussions. JYC also acknowledges an NSF-DMR0756281 and the Alfred P Sloan Fellowship for partial support of this project. DPY acknowledges an NSF-CAREER award (DMR0449022). PWA acknowledges the support of DOE under Grant No. DE-FG02-07ER46420. The authors are grateful to the Materials Design and Characterization Laboratory of the Institute of Solid State Physics at the University of Tokyo. This work was partly supported by Grants-in-Aid for Scientific Research (21684019)

from JSPS, Scientific Research on Priority Areas (17071003) and Scientific Research on Innovative Areas ‘Heavy Electrons’ (20102007) from MEXT of Japan.

References

- [1] Florio J V, Rundle R E and Snow A I 1952 *Acta Crystallogr.* **5** 449–57
- [2] Gladyshevskii E I, Kripyakevich P I, Teslvuk M Y, Zarechnyuk O S and Kuz'ma Y B 1961 *Kristallografiya* **6** 267–8
- [3] Christides C, Kostikas A, Zouganelis G, Psyharis V, Kou X C and Grossinger R 1993 *Phys. Rev. B* **47** 11220–9
- [4] Coldea M, Neumann M, Lutkehoff S, Mahl S and Coldea R 1998 *J. Alloys Compounds* **278** 72–9
- [5] Dmitriev V M, Stepien-Damm J, Suski W, Talik E and Prentslau N N 2004 *Phys. Status Solidi c* **1** 1824–7
- [6] Dmitriev V M, Terekhov A V, Suski W, Ishchenko L A, Cwik J, Palewski T, Kotur B Y and Talik E 2008 *J. Alloys Compounds* **452** 217–24
- [7] Gottwick U, Held R, Sparr G, Steglich F, Vey K, Assmus W, Rietschel H, Stewart G R and Giorgi A L 1987 *J. Magn. Magn. Mater.* **63/64** 341–3
- [8] Kotur B Y, Palasyuk A M, Bauer E, Michor H and Hilscher G 2001 *J. Phys.: Condens. Matter* **13** 9421–31
- [9] Leavey C J, Rainford B D, Stewart J R and Adroja D T 2007 *J. Magn. Magn. Mater.* **310** 1041–3
- [10] Moze O, Caciuffo R, Li H S, Hu B P, Coey J M D, Osborn R and Taylor A D 1990 *Phys. Rev. B* **42** 1940–3
- [11] Paci B, Caciuffo R, Amoretti G, Moze O, Buschow K H J and Murani A P 1995 *Solid State Commun.* **94** 489–93
- [12] Yamasaki T, Matsui K, Nakamura H and Shiga M 2001 *Solid State Commun.* **119** 415–8
- [13] Gladyshevskii E I, Kripyakevich P I, Cherkashin E E, Zarechnyuk O S, Zalutskii I I and Evdokimenko V I 1963 *Redkozem. Elem.* **67**
- [14] Landelli A and Palenzona A 1965 *J. Less-Common Met.* **9** 1–6
- [15] Suski W, Gschneidner K A Jr and LeRoy E 1996 *The ThMn₁₂-Type Compounds of Rare Earths and Actinides: Structure, Magnetic and Related Properties* vol 22, ed K A Gschneidner Jr and L Eyring (Amsterdam: Elsevier) chapter 149, pp 143–294
- [16] Wang F E and Gilfrich J V 1966 *Acta Crystallogr.* **21** 476–81
- [17] Hagmusa I H, Klaasse J C P, Bruck E, de Boer F R and Buschow K H J 2001 *J. Alloys Compounds* **314** 37–41

- [18] Baio G, Moze O, Amoretti G, Sonntag R, Stusser N and Buschow K H J 1997 *Z. Phys. B* **102** 449–53
- [19] Felner I and Nowik I 1979 *J. Phys. Chem. Solids* **40** 1035–44
- [20] Rauchschalbe U, Gottwick U, Ahlheim U, Mayer H M and Steglich F 1985 *J. Less-Common Met.* **111** 265–75
- [21] Ido H, Nishioka T and Kontani M 1998 *J. Magn. Magn. Mater.* **177–181** 385–6
- [22] Kontani M, Hamada M, Mizukoshi T and Mukai H 2000 *Physica B* **284–288** 1267–8
- [23] Oe K, Kobayashi R, Nishioka T, Kato H, Matsumura M and Kodama K 2009 *J. Phys.: Conf. Ser.* **150** 042146
- [24] Lue C S, Su T H and Lai W J 2006 *J. Magn. Magn. Mater.* **304** e445–e7
- [25] Buschow K H J 1991 *J. Magn. Magn. Mater.* **100** 79–89
- [26] Caciuffo R, Amoretti G, Buschow K H J, Moze O, Murani A P and Paci B 1995 *J. Phys.: Condens. Matter* **7** 7981–9
- [27] De Boer F R, Ying-Kai H, De Mooij D B and Buschow K H J 1987 *J. Less-Common Met.* **135** 199–204
- [28] De Mooij D B and Buschow K H J 1988 *J. Less-Common Met.* **136** 207–15
- [29] Sheldrick G M 2008 *Acta Crystallogr. A* **64** 112
- [30] Haucke W 1940 *Z. Anorg. Allg. Chem.* **244** 17–22
- [31] Mason J T, Harsha K S and Chiotti P 1970 *Acta Crystallogr. B* **26** 356–61
- [32] Hu B P, Li H S and Coey J M D 1990 *J. Appl. Phys.* **67** 4838–40
- [33] Yang Y, Sun H, Kong L, Yang J, Ding Y, Zhang B, Ye C, Jin L and Zhou H 1988 *J. Appl. Phys.* **64** 5968–70
- [34] Bessais L and Djega-Mariadassou C 2001 *Phys. Rev. B* **63** 054412
- [35] Barandiaran J M, Gignoux D, Rodriguez-Fernandez J and Schmitt D 1989 *Physica B* **154** 293–9
- [36] Bobev S, Fritsch V, Thompson J D and Sarrao J L 2006 *J. Solid State Chem.* **179** 1035–40